Heliyon 5 (2019) e02169

Contents lists available at ScienceDirect

Heliyon

www.elsevier.com/locate/heliyon

Vision-based lane departure warning framework

Em Poh Ping [a,*], J. Hossen [a], Fitrian Imaduddin [b], Wong Eng Kiong [a]

[a] *Faculty of Engineering and Technology, Multimedia University, Jalan Ayer Keroh Lama, Bukit Beruang, 75450 Melaka, Malaysia*
[b] *Faculty of Engineering, Universitas Sebelas Maret, Jalan Ir. Sutami 36A, Kentingan, Surakarta 57126, Central Java, Indonesia*

ARTICLE INFO

Keywords:
Computer science
Vision-based
Lane departure detection
Lateral offset ratio
Lane detection
Lane departure warning framework

ABSTRACT

Collisions arising from lane departures have contributed to traffic accidents causing millions of injuries and tens of thousands of casualties per year worldwide. Many related studies had shown that single vehicle lane departure crashes accounted largely in road traffic deaths that results from drifting out of the roadway. Hence, automotive safety has becoming a concern for the road users as most of the road casualties occurred due to driver's fallacious judgement of vehicle path. This paper proposes a vision-based lane departure warning framework for lane departure detection under daytime and night-time driving environments. The traffic flow and conditions of the road surface for both urban roads and highways in the city of Malacca are analysed in terms of lane detection rate and false positive rate. The proposed vision-based lane departure warning framework includes lane detection followed by a computation of a lateral offset ratio. The lane detection is composed of two stages: pre-processing and detection. In the pre-processing, a colour space conversion, region of interest extraction, and lane marking segmentation are carried out. In the subsequent detection stage, Hough transform is used to detect lanes. Lastly, the lateral offset ratio is computed to yield a lane departure warning based on the detected *X*-coordinates of the bottom end-points of each lane boundary in the image plane. For lane detection and lane departure detection performance evaluation, real-life datasets for both urban roads and highways in daytime and night-time driving environments, traffic flows, and road surface conditions are considered. The experimental results show that the proposed framework yields satisfactory results. On average, detection rates of 94.71% for lane detection rate and 81.18% for lane departure detection rate were achieved using the proposed frameworks. In addition, benchmark lane marking segmentation methods and Caltech lanes dataset were also considered for comparison evaluation in lane detection. Challenges to lane detection and lane departure detection such as worn lane markings, low illumination, arrow signs, and occluded lane markings are highlighted as the contributors to the false positive rates.

1. Introduction

Crashes due to lane departures account for the majority of highway fatalities and caused hundreds of human deaths, thousands of injuries, and billions of dollars in losses each year. It is reported in Jacobs and Aeron-Thomas (1999); Jacobs et al. (2000) that Malaysia has been ranked as the country with the highest fatalities per 100,000 of population in the world since 1996. From a global point of view, in 1999 the regional distribution of the 750,000 annual fatalities places almost half of them in Asia (Jacobs and Aeron-Thomas, 1999; Jacobs et al., 2000). A similar proportion of road fatalities in Asia holds for 2014 (Al-Madani, 2018). Furthermore, the road fatalities statistical data found in Al-Madani (2018); Jacobs and Aeron-Thomas (1999) shows an increasing trend in worldwide traffic fatalities, which agrees with the predicted future development of road fatalities in different regions of the world (Kopits and Cropper, 2005; Wegman, 2017). Particularly in the region of South Asia, the predicted number of road fatalities for 2020 is more than 3.5 times higher than the total road fatalities recorded in 1990.

In response to this problem, Lane Keeping Assistance (LKA) (Yoshida et al., 2015); Lane Departure Warning (LDW) (Haloi and Jayagopi, 2015; Narote et al., 2018; Viswanath et al., 2016); Lane Following (LF) (Jung and Kelber, 2004, 2005b); Lateral Control (LC); Intelligent Cruise Control (ICC); Collision Warning (CW) (Meng and Spence, 2015), and Autonomous Vehicle Guidance (Vacek et al., 2007) have been called for by vehicle manufacturers to enhance vehicle safety.

In general, research on LDW can be divided into two classes. The first consists of those without control units, such as LDW and collision warning (CW). This passive safety system only collects information and

* Corresponding author.
E-mail address: ppem@mmu.edu.my (P.P. Em).

https://doi.org/10.1016/j.heliyon.2019.e02169
Received 19 January 2019; Received in revised form 28 March 2019; Accepted 24 July 2019

sends a warning or reminder if necessary. These systems are usually implemented in Driving Assistant System (DAS), instead of in vehicles as part of autonomous vehicle guidance. The second type of system is designed with feedback, namely, an active safety system, and with the aim of affecting the vehicle's behaviour, which functions as a controller.

In the present paper, a passive type of LDW is proposed: a vision-based lane departure warning (VBLDW) framework. VBLDW includes vision-based lane detection (VBLD) followed by the computation of the lateral offset ratio (LOR). VBLD is composed of a pre-processing stage followed by a detection stage. The pre-processing stage of VBLD is made up of colour space conversion, region-of-interest extraction, and lane marking segmentation. The finite impulse response saturation autothreshold (FIRSA) lane marking segmentation method used in this paper is implemented by a 2D-Finite impulse response (2D-FIR) filter followed by a saturation function and autothreshold. The detection stage of VBLD is formed by the Hough transformation and peak detection, reverse Hough transformation, and the drawing of the lines detected in the original image. For performance evaluation of VBLDW, clips from real-life datasets have been used to evaluate the lane boundary detection rate and the lane departure detection rate.

The rest of this paper is organized as follows. Section 2 begins with the introduction of VBLDW, which presents VBLD in subsection 2.1 and the LOR in subsection 2.2. The experimental test bed and real-life datasets are presented in Section 3, where the camera used in this work is described in subsection 3.1 and the real-life datasets are presented in subsection 3.2. The experimental results and a discussion are presented in Section 4. Some conclusions and some avenues for future research are presented in Section 5.

2. Methodology

As an essential part of an Intelligent Transport System (ITS), LDW plays a vital role in reducing road fatalities by giving a lane departure warning to drivers for any unintended lane departures. The proposed VBLDW is based on VBLD. 'Lane departure' means that a travelling vehicle is departing from its current lane or has a tendency to go across a lane boundary. As a result, the driver or monitoring system will see only one lane boundary moving towards the middle horizontally in the front view. Based on this fact, a lane departure can be determined by checking the horizontal position of each lane boundary (Lu, 2015), which correspond to the X-coordinates of the bottom end-points of the lane boundary in the image plane. A warning is issued by the system when the vehicle comes within a defined distance from the lane boundary. Fig. 1 shows a flow chart involving VBLD and the proposed VBLDW. In this section, the method of VBLD is introduced first in subsection 2.1, which is then followed by a description of the LOR for the proposed VBLDW in subsection 2.2.

2.1. Vision-based lane detection

VBLD was developed in MATLAB Simulink. Basically, it has two stages: pre-processing and detection. The pre-processing stage has three main components: colour space conversion, a Region of Interest extraction, and FIRSA lane marking segmentation, in that order. The pre-processing stage uses the input image (Step 1 in Fig. 1) from a Logitech C525 camera Logitech (2018), which is fixed at the centre of the front windscreen to capture road footage (Sternlund et al., 2017; Sudhakaran, 2017). For simplicity, the camera is assumed to be set up so as to make the baseline horizontal, which ensures that the horizon is in the image and is parallel to the X-axis of the image plane. In this paper, it is assumed that the resolution of the image input to the pre-processing stage is 320×180 Red, Green, Blue (RGB).

The initial step is to convert the input RGB colour image to greyscale (Step 2 in Fig. 1). The reason for this is to reduce the processing time by lessening the amount of data to be processed. Equation (1) represents the function which is to be applied to the RGB image for this conversion.

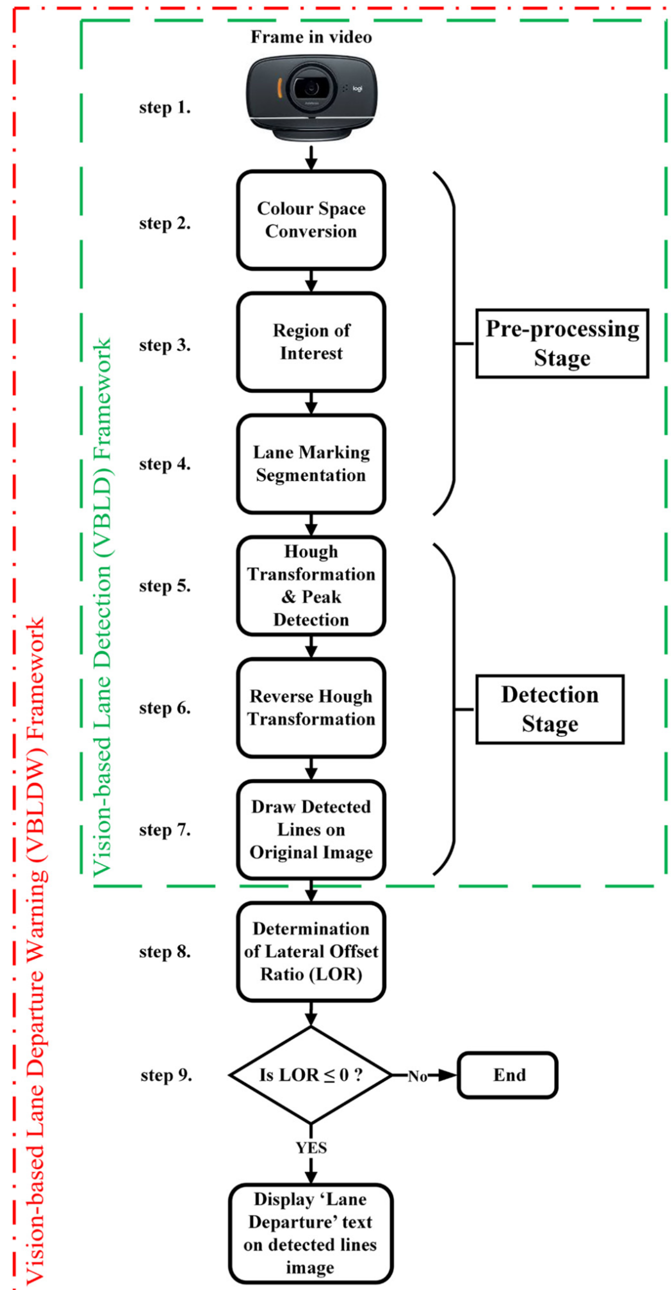

Fig. 1. Flow chart for vision-based lane detection and vision-based lane departure warning.

The original image from frame 1 of clip #1 is shown in Fig. 2, while Fig. 3 shows the converted greyscale image.

$$\text{Greyscale} = \begin{bmatrix} 0.299 & 0.587 & 0.114 \end{bmatrix} \begin{bmatrix} R' \\ G' \\ B' \end{bmatrix} \tag{1}$$

Where

R' - Red component of the image.
G' - Green component of the image.
B' - Blue component of the image.

The reason for employing a pre-processing stage is because the images in videos taken in the real world contain significant outliers other than the actual lane markings. The images need to be properly prepared

Fig. 2. Original frame 1 image from clip #1.

Fig. 3. RGB to greyscale conversion of the original frame 1 image from clip #1.

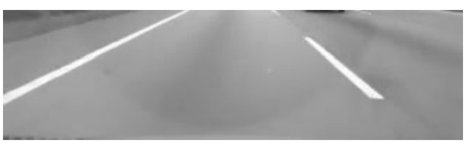

Fig. 4. Region of Interest in greyscale of the original frame 1 image from clip #1.

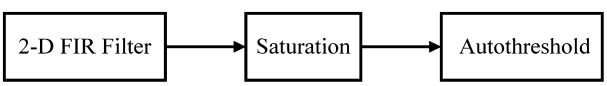

Fig. 5. Flow chart of Finite Impulse Response Saturation Autothreshold lane marking segmentation.

with outliers filtered out, depending on the requirements of different computer vision systems. This can be accomplished by extracting a Region of Interest (ROI) and then applying a lane marking segmentation. Fig. 4 shows the greyscale image after extracting the ROI from the original image. One can see that the bottom half of the image has been selected as the ROI (Narote et al., 2018) (Step 3 in Fig. 1). Usually, the upper region of the image is considered to contain outliers due to unwanted features such as vehicles, road signs, and roadside trees. The image resolution of the ROI is reduced to 320×90.

The flow chart of the FIRSA lane marking segmentation method has three main blocks: a 2-Dimensional Finite Impulse Response (2-D FIR) filter, a Saturation block, and an Autothreshold block, as illustrated in Fig. 5. It is applied in Step 4 of VBLD, as shown in Fig. 1. The 2-D FIR filter is a basic filter for image processing, and is used to support edge extraction (Chandrasekar and Ryu, 2016) and noise removal (Shah, 1997). Edge extraction is essential in image processing because edges represent a significant portion of the characteristics contained in an image, such as, in the context of lane detection, the lane markings painted on the road surface. In this paper, a 2-D FIR filter (Terrell and Simpson, 1986) is used to extract these lane markings. The 2-D FIR edge extraction is designed for regions where the light intensity changes slowly. It can determine an edge and smooth the noise in a noisy image, simultaneously. It is also computationally more efficient than the popular Laplacian of Gaussian method (Shah, 1997).

As in Terrell and Simpson (1986), a 2-D FIR filtering operation in spatial convolution may be carried out be using a neighbourhood averaging method, where the $H(i,j)$ pixel value is changed to the $C(i,j)$

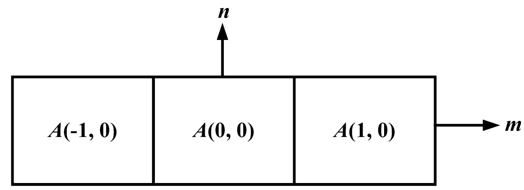

Fig. 6. Discrete spatial coordinates of the filter kernel.

pixel value, as shown in Equation (2). In Equation (2), A denotes the filter kernel and $*$ denotes the operation of convolution. The edge detection filter kernel in this case is 1×3 and each pixel in the filter kernel is as shown in Equation (3).

$$C(i,j) = \sum_{m=0}^{(Ma-1)} \sum_{n=0}^{(Na-1)} A(m,n) * H(i-m, j-n) \tag{2}$$

$$A = \begin{bmatrix} -1 & 0 & 1 \end{bmatrix} \tag{3}$$

where $0 \le i < Ma + Mh - 1$ and $0 \le j < Na + Nh - 1$ for full output size; replicate padding is applied for the reference pixels outside the image boundary. $C(i,j)$ is the filtered image, $H(i,j)$ is the ROI greyscale image, A is the filter kernel, m, n are the discrete spatial coordinates of the filter kernel, Ma, Na are the original image dimensions, and Mh, Nh are the filter kernel dimensions. Suppose that the filter kernel pixels are given as shown in Fig. 6 and every pixel of the filter kernel is assumed to satisfy $-1 \le m \le 1$. Since the filter kernel in Equation (3) is a single row filter kernel, Equation (2) can be reduced to Equation (4).

$$C(i,j) = \sum_{m=-1}^{m=1} A(m,n) * H(i-m, j) \tag{4}$$

Figs. 7a-7b show the input ROI greyscale image and the surface plot of the input ROI greyscale image for frame 1 of clip #1, respectively. An irregularity is observed in the input ROI greyscale image surface plot, as shown in Fig. 7b), due to unwanted noise appearing on the road surface and side road. Still, the lane markings appear as white pixels in Fig. 7a and can be translated as the peaks in the Z-axis of the surface plot in Fig. 7b. In order to remove unwanted noise pixels appearing in the input ROI greyscale image and distinctly extract the lane markings, the 2-D FIR filter is then applied to the input ROI greyscale image. Figs. 7c-7d show the filtered image and the surface plot of filtered image for frame 1 of clip #1, respectively. From the filtered image and surface plot of the filtered image, it can be seen that the lane markings white pixels in Fig. 7c clearly stand out from the rest of the image pixels, which translates into distinct peaks with the flat reference surface at zero intensity in Fig. 7d. Still, non-positive distinct peaks are observed in the surface plot of the filtered image in Fig. 7d due to the $[-1\ 0\ 1]$ filter kernel used in 2-D FIR. Hence, in order to remove the non-positive distinct peaks appearing in Fig. 7d, a saturation is applied to the filtered image, as shown in the flow chart of the FIRSA lane marking segmentation method in Fig. 5.

The output signal of the 2-D FIR is connected to a saturation block, as shown in Fig. 5, which produces an output signal that is the value of the input signal bounded to the upper saturation value of (1) and lower saturation value of (0). The specified upper and lower limits are used to saturate the unwanted range of signals ($C(i,j) < 0$). Figs. 7e-7f show the saturated image and the surface plot of the saturated image for frame 1 of clip #1, respectively. It can be seen that the non-positive distinct peaks have been saturated to a reference intensity value of (0). The saturated signals are then connected to the autothreshold block, as shown in Fig. 5.

The autothreshold block in the flow chart of FIRSA lane marking segmentation method as shown in Fig. 5 is a binarization step, which is required to highlight the lane marking of the filtering images. The core problem of binarization is how to determine the optimal threshold: if the threshold is excessively large, then a lane edge point will be

(a) Input Region on Interest greyscale image

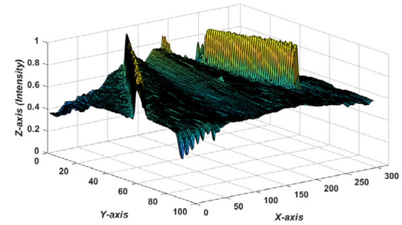

(b) Surface plot of greyscale image

(c) Filtered image

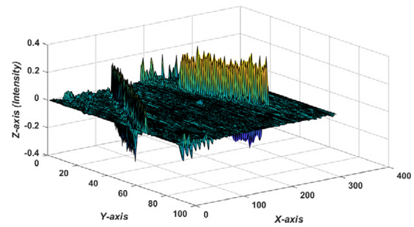

(d) Surface plot of filtered image

(e) Saturated image

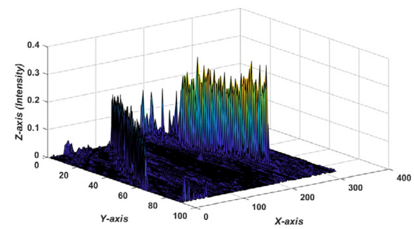

(f) Surface plot of saturated image

Fig. 7. Images (a), (c), and (e) represent the input Region of Interest greyscale image, filtered image, and saturated image for frame 1 of clip #1, respectively. Images (b), (d), and (f) represent the surface plot of the greyscale image, the surface plot of the filtered image, and the surface plot of the saturated image for frame 1 of clip #1, respectively.

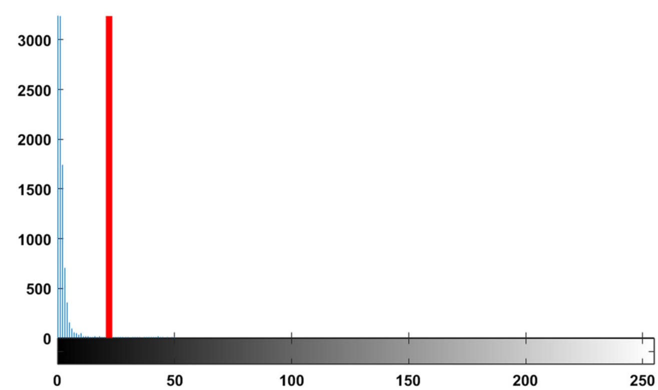

Fig. 8. Histogram and a normalized threshold (red solid line) for the filtered frame 1 of clip #1.

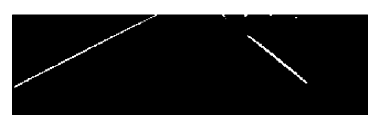

Fig. 9. Thresholded image for filtered frame 1 of clip #1.

missed or some redundant information will be detected. The FIRSA lane marking segmentation method employs Otsu thresholding for the binarization (Otsu, 1979). In Otsu thresholding, the histogram of the image pixel values is examined so as to choose a threshold automatically. The idea of Otsu thresholding is to search for two peaks: one representing a foreground pixel value and one representing a background pixel value, and choose a point in between these two peaks as the threshold value. Frame 1 of the filtered clip #1 is chosen and Otsu thresholding is applied to get a normalized threshold value. Then, the normalized threshold value (red solid line) is plotted together with the histogram for the filtered frame 1 of clip #1 as shown in Fig. 8. The thresholded image is shown in Fig. 9.

The Hough transform (HT) Duda and Hart (1972) is a technique that recognizes a specific configuration of points in an image, such as a lane segment, curve, or other pattern. The fundamental principle is that the form sought may be expressed via a known function depending on a set of parameters. A particular instance of the form sought is therefore entirely specified by the values taken by such a set of parameters.

For example, by taking Equation (5) as the representation of straight lanes, any straight lane is entirely specified by the value of the parameters (a, b). Equivalently, if one takes a different type of representation, as in Equation (6), the straight lane is completely specified by the pair (ρ, θ).

$$Y = aX + b \tag{5}$$

$$\rho = X\cos(\theta) + Y\sin(\theta) \tag{6}$$

For illustrating the detection stage operation, the edge detection is performed on frame 1 of clip #1, shown in Fig. 9, in order to find the left and right edges of the segmented lane markings in the binary image. In this paper, a standard Hough transformation is used for the edge detection of the lane markings (Step 5 in Fig. 1). Fig. 10 shows the result of the Hough transformation in the parameter plane for frame 1 of clip #1 image with theta, θ. The resolution is set to $\pi/180$ radians and the ρ resolution is configured to 1. The range of θ is set to -1.2217 radians to 1.1868 radians. Local maxima detection is applied to the parameter plane to extract the peaks that correspond to the left and right lane boundaries (Step 5 in Fig. 1). Fig. 10 shows the results of this local maxima detection, with the highlighted two red squares indicating the

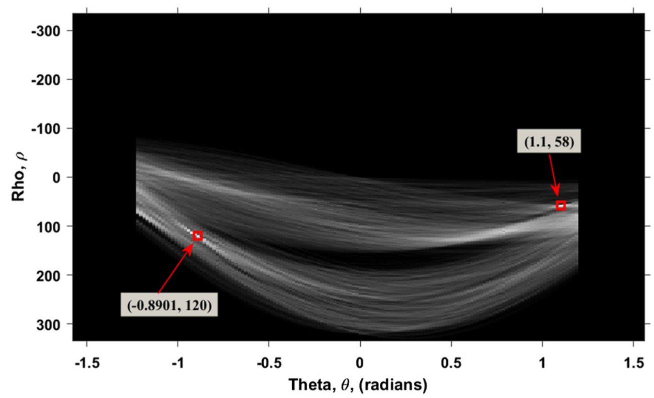

Fig. 10. Hough transformation and Hough peaks (two red squares) in parameter plane for frame 1 of clip #1.

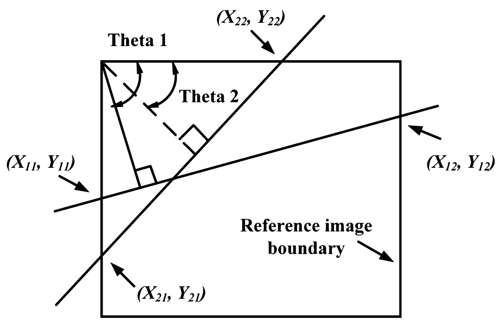

Fig. 11. Example of intersection of Hough lines.

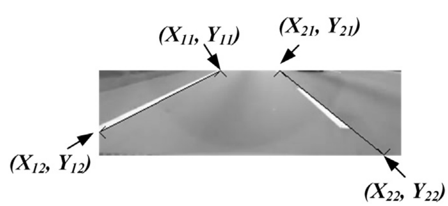

Fig. 12. Hough lines of the Region of Interest greyscale image for frame 1 of clip #1.

right and left lane boundaries at $(-0.8901, 120)$ and $(1.1, 58)$. The configuration for the extraction of the local maxima is that two local maxima are sought, the neighbourhood size is [319 89], and the threshold is 1.

A reserve Hough transformation is carried out on the Hough peaks in order to display the detected lane boundaries for frame 1 of clip #1 (Step 6 in Fig. 1). This step involves the identification of the Cartesian coordinates of the intersection of the reference image boundary lines and the lines described by constant pairs (ρ, θ). Fig. 11 shows an example of Line 1 intersecting the boundaries of the reference image at $[(X_{11}, Y_{11})\ (X_{12}, Y_{12})]$ and Line 2 intersecting the boundaries at $[(X_{21}, Y_{21})\ (X_{22}, Y_{22})]$. The Cartesian coordinates of (X_{11}, Y_{11}), (X_{12}, Y_{12}), (X_{21}, Y_{21}), and (X_{22}, Y_{22}) can be calculated from Equation (6). Fig. 12 shows the results of the reverse Hough transformation applied to the ROI greyscale image for frame 1 of clip #1 as the ground truth. The image boundary intersection points are highlighted in a black 'X-mark' with the solid black lines representing the Hough lines, as shown in Fig. 12. Both of the Hough lines are in line with the ground truth for the left and right lane boundaries. The $(-0.8901, 120)$ Hough peak indicates the left lane boundary and the $(1.1, 58)$ Hough peak indicates the right lane boundary.

The Cartesian coordinates for (Y_{11}), (Y_{12}), (Y_{21}), and (Y_{22}) are required to be extended for another 90 pixels vertically due to the selection of the bottom half of the image as the ROI. The Cartesian coordinates for (X_{11}, Y_{11}) and (X_{12}, Y_{12}) are linked with an overlay red line

Fig. 13. Correct lane detection for frame 1 of clip #1.

that corresponds to the left lane boundary (Step 7 in Fig. 1). The Cartesian coordinates for (X_{21}, Y_{21}) and (X_{22}, Y_{22}) are linked with an overlay red line that corresponds to the right lane boundary (Step 7 in Fig. 1). Both overlaid red lines show a correct lane detection for the original image for frame 1 of clip #1, as shown in Fig. 13.

2.2. Lateral offset ratio

The lateral offset of the vehicle with respect to the centre of the lane has been used to predict lane departure, as in Risack et al. (2000); Marino et al. (2009). However, the existing techniques depend on some kind of camera calibration procedure to obtain the offset, while the proposed VBLDW framework does not require any intrinsic or extrinsic camera parameters (Jung and Kelber, 2005a). In this paper, both X-coordinates of the bottom end-points (X_{12} and X_{22}) of the lane boundary in the image plane, as described in subsection 2.1, will be analysed for each frame for the computation of the LOR (Step 8 in Fig. 1):

$$\mathrm{LOR} = \frac{\min\left[\left\{\left|X_{22} - X_m\right|\right\}, \left\{\left|X_m - X_{12}\right|\right\}\right] - T_H X_m}{T_H X_m} \tag{7}$$

where T_H is the lane departure warning threshold, set to a constant value of 0.8, X_{12} is the detected left bottom end-point of the right lane boundary, X_{22} is the detected right bottom end-point of the right lane boundary, and X_m is one-half of the horizontal width of the image plane. Based on ISO 17361:2007 (International Organization for Standardization [ISO], 2007), there is no specification of how early the warning threshold should be made before crossing the lane. However, there is a warning threshold reference provided in ISO 17361:2007 (International Organization for Standardization [ISO], 2007), which states that the reference warning threshold is placed roughly at 80% of the lane width from the centre of the lane boundary. The absolute value $|X_m - X_{12}|$ indicates the horizontal pixel distance between the detected X_m and X_{12} in the image plane. The absolute value $|X_{22} - X_m|$ indicates the horizontal pixel distance between the detected X_{22} and X_m in the image plane. The min function is used to select the minimum element of $|X_m - X_{12}|$ and $|X_{22} - X_m|$ for each frame. The difference between the selected minimum element and $T_H X_m$ indicates the horizontal pixel distance between the warning threshold and the detected X_{12} or X_{22}. Hence, the LOR is defined as the ratio between the horizontal pixel distance between the warning threshold and the detected X_{12} or X_{22} and the horizontal pixel distance between the warning threshold and X_m. The projection of a road in the image plane for determining the LOR can be seen in Fig. 14.

If the vehicle is travelling parallel to the lane boundaries and exactly at the centre of the lane, then the LOR as a function of the left bottom end-point of the left lane boundary, X_{12}, the right bottom end-point of the right lane boundary, X_{22}, one-half the horizontal width of the image plane, X_m, and the warning threshold, T_H, will be constant and equal to 0.25. If the vehicle is travelling parallel to the lane boundaries but displaced from the centre of the lane, LOR will still be constant, but with a value smaller than 0.25 (in fact, this value can be close to −1 if the vehicle is close to a lane boundary). In this case, no lane departure warning signal should be triggered, because the vehicle does not appear to be leaving its lane. If the vehicle is travelling towards a lane boundary

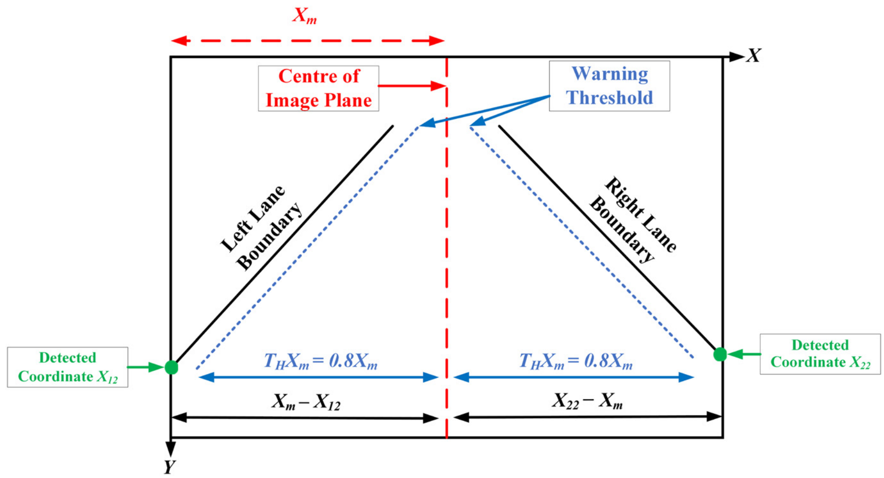

Fig. 14. Projection of a road in image plane.

Table 1
Lane departure identification using lateral offset ratio.

LOR	Lane Departure Identification
LOR = 0.25	No lane departure
$0 < \text{LOR} \leq 0.25$	No lane departure
LOR = 0	Lane Departure
$-1 \leq \text{LOR} \leq 0$	Lane departure
LOR = −1	Lane Departure

from the centre of the lane, LOR will decrease from 0.25 to −1. In this case, a lane departure warning signal should be triggered, because the vehicle appears to be leaving its lane. Hence, the 'Lane Departure' text is displayed in the sequence of images in video clip #5, as shown in Figs. 15b-15h.

Table 1 shows the lane departure identification using LOR (Step 9 in Fig. 1). LOR ranges from −1 to 0.25. The range of values of LOR for a lane departure zone is $-1 \leq \text{LOR} \leq 0$. In addition, a LOR value equal to zero indicates the vehicle is crossing the warning threshold. Hence, a lane departure warning signal is issued. The range of values of LOR for the no lane departure zone is $0 < \text{LOR} \leq 0.25$ with the maximum value of LOR indicating that the vehicle is located at the centre of the lane. Hence, no lane departure warning signal is issued. The minimum value of LOR = −1 indicates that the vehicle is crossing one of the lane boundaries. Hence, a lane departure warning signal is issued.

Fig. 16 shows the LOR and lane departure detection ($\text{LOR} \leq 0$) for the sequence of images at intervals of 20 frames of video clip #5 that were used in Fig. 15. Fig. 16 illustrates the sequence of images of a right departing vehicle. At frame 5600 of clip #5, as shown in Fig. 15a, the LOR has a value of 0.1875, which reflects the fact that the vehicle is still within the no lane departure zone (LOR > 0). Hence, there is no 'Lane Departure' text displayed in frame 5600. At frame 5620 of clip #5 as shown in Fig. 15b, the LOR is equal to −0.0234, which reflects the fact that the vehicle has moved from the centre of the lane and crossed the warning threshold ($\text{LOR} \leq 0$). Hence, the text 'Lane Departure' is displayed in frame 5620. For frames 5640 and 5660 as shown in Figs. 15c-15d, a decreasing trend of LOR values (−0.3281 to −0.7266) is observed in Fig. 16, which reflects the fact that the vehicle is going to cross the lane boundary and is still in the lane departure zone ($\text{LOR} \leq 0$). Hence, the text 'Lane Departure' is displayed in frames 5640 and 5660.

For frames 5680 to 5720 in Figs. 15e-15g, an increasing trend of LOR (−0.8281 to −0.4688 to −0.1719) is observed in Fig. 16, which reflects the fact that the vehicle has just crossed the lane boundary and is still moving within the lane departure zone ($\text{LOR} \leq 0$). Hence, the text 'Lane Departure' is displayed in frames 5680, 5700, and 5720. For frame 5740 as shown in Fig. 15h, the LOR is 0, which reflects the fact that the vehicle is crossing the warning threshold (LOR = 0). Hence, the text 'Lane Departure' is displayed in frame 5740. For frames 5760 and 5780 as shown in Figs. 15i-15j, the LOR is 0.0547 and 0.0781, which reflects the fact that the vehicle is located within the no lane departure zone (LOR > 0). Hence, there are no 'Lane Departure' texts displayed in frames 5760 and 5780.

3. Instrumentation

The proposed VBLDW has been implemented with MATLAB and Simulink, under the operating system Windows 10, using Intel 4 cores @ 1.6GHz processor and 4 GB RAM. Fig. 17 shows the flow chart of road footage acquisition in off-line mode so that trimming could be done on the video clip footage before running the proposed VBLDW simulation. The experimental test bed is shown in Fig. 18 and a schematic diagram for the camera position is shown in Fig. 19.

3.1. Logitech C525 camera

The video sensing device that was used to collect the road footage was Logitech C525 (Logitech, 2018). This camera was attached to the front windscreen at a height of 1.045 m above the ground and located at the centre of the windscreen, as shown in Fig. 19. The frame rate of the road footage is 30 frames per second (FPS). Since the frame size has an enormous impact on the total speed of the system, the image resolution was reduced to 320×180 after being captured from the camera, for real-time image processing.

3.2. Real-life datasets

The real-life datasets of road footages were acquired in the same rate (30 Hz) and trimmed into corresponding clip numbering as presented in Tables 2, 3 for daytime and night-time driving environments, respectively. Real-life datasets contained road footages of daytime and night-time driving environments in urban roads and highway. Table 2 shows the descriptions of captured daytime road footage clips on urban roads except clip #1 on highway, which contained multiple occurrences of lane departure. Road surface conditions such as worn lane markings, glare, reflections, wet, other road markings like arrow marks, and occluded lane markings during daytime driving environment were observed.

Table 3 shows the descriptions of captured night-time road footage clips on urban roads except clip #14 on highway, which contained multiple occurrences of lane departure. Road surface conditions such as worn lane markings, night glare, other road markings like arrow marks, and occluded lane markings during night-time driving environment are

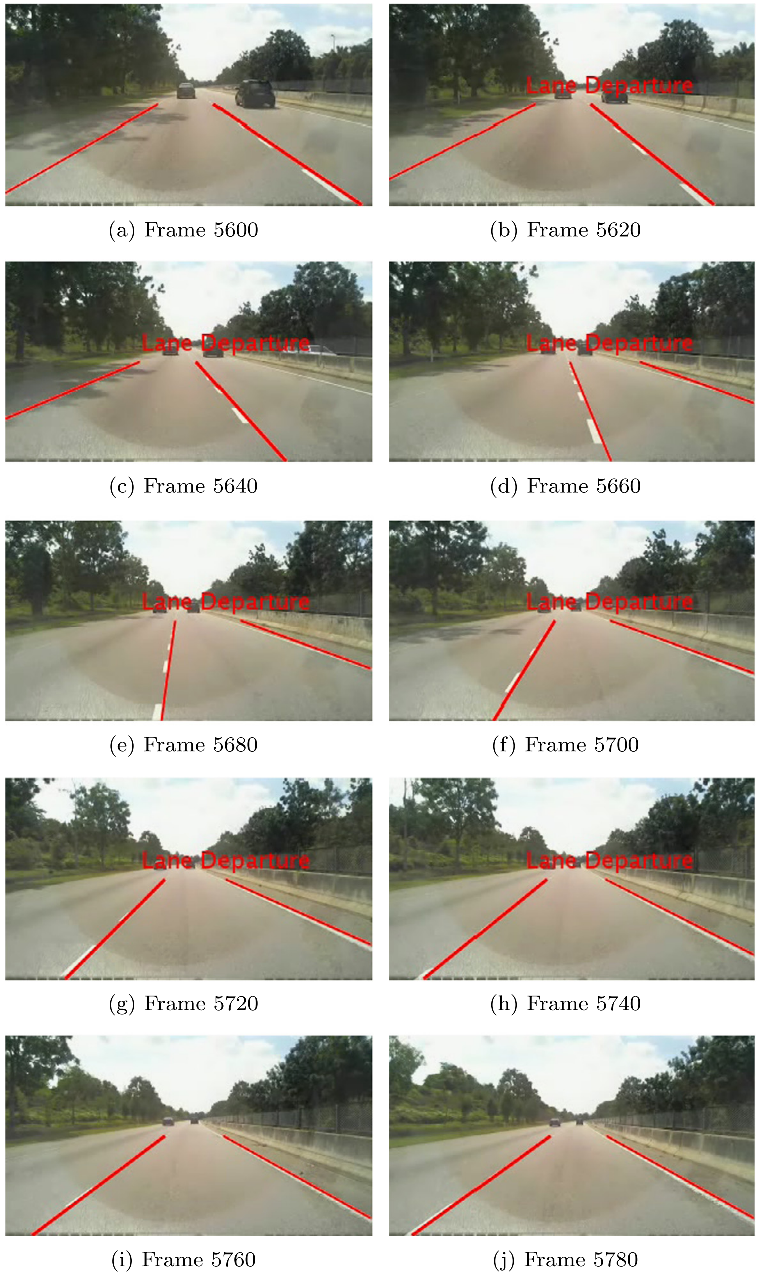

Fig. 15. Sequence of images in video clip #5 demonstrating the detected lane departure.

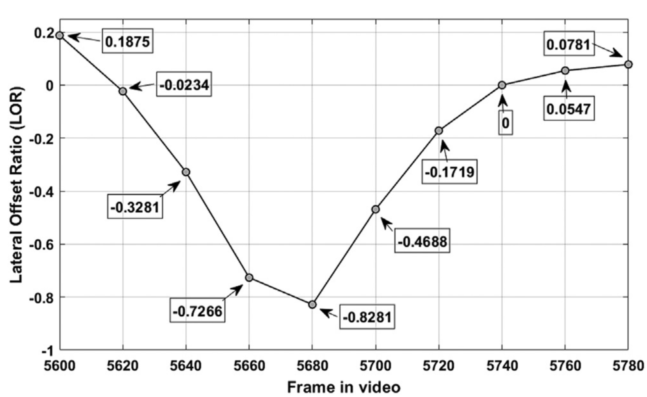

Fig. 16. Lateral offset ratio and lane departure detection (LOR ≤ 0) for the sequence of images in video clip #5 as shown in Fig. 15.

also considered in the experiment investigation. The evaluation will be done in frame by frame basic (Cualain et al., 2012). In total, the real-life datasets contained approximately 69964 frames and 237998 lane boundaries under daytime and night-time driving environments.

4. Results & discussion

The effectiveness of VBLD and VBLDW are investigated in this section. The real-life datasets shown in Tables 2, 3 contained all three test scenarios, namely straight road, curved road, and false alarms. The performance of VBLD and VBLDW in lane detection and lane departure detection will be evaluated under daytime and night-time driving environments. The lane detection results for VBLD will be compared with the existing lane detection algorithms reported in the literature. Whereas, the overall lane departure detection results for VBLDW is presented. The performance evaluation of lane detection and lane departure detection are summarised in subsection 4.1. While, the comparison

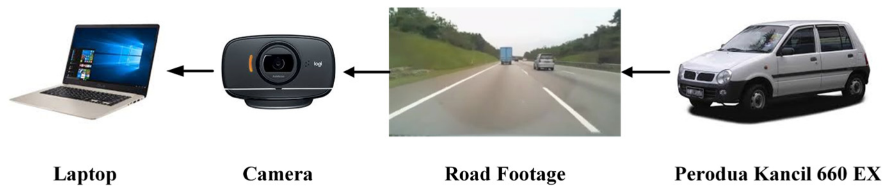

Fig. 17. Test bed for acquiring real-life datasets.

Fig. 18. The experimental setup.

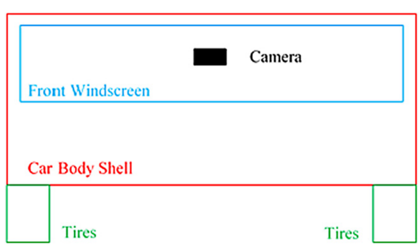

Fig. 19. Attached camera position in sectional view.

of lane detection results and overall lane departure detection results for VBLDW are summarised in subsection 4.2.

4.1. Performance evaluation of lane detection and lane departure detection

The lane detection results under daytime and night-time driving environments are presented in Tables 4, 5, respectively. In order to evaluate the performance of VBLD, the number of lanes per frame, the number of detected lanes per frame, the number of correctly detected lanes per frame, and the number of false positive lanes per frame, were manually counted on a frame to frame basis. Equations (8), (9), and (10) present the formulas used for the total number of detected lanes, the detection rate, and the false positive rate, respectively.

$$N_T = N_D + N_F \tag{8}$$

$$\text{Lane detection rate} = \frac{N_D}{N_T} \times 100\% \tag{9}$$

$$\text{False positive rate in lane detection} = \frac{N_F}{N_T} \times 100\% \tag{10}$$

Where

N_T - Total number of detected lane.
N_D - Total number of correctly detected lane.
N_F - Total number of false positive lane.

In clips #1-#13, 96.45%, 86.17%, 97.53%, 91.20%, 93.74%, 97.27%, 94.57%, 97.37%, 96.97%, 98.24%, 97.21%, 98.04% and 77.99% of 3892, 6592, 8992, 3112, 14094, 4800, 16796, 5100, 7500, 4200, 4200, 5039, and 1077 lanes were detected correctly with 3.55%, 13.83%, 2.47%, 8.80%, 6.26%, 2.73%, 5.43%, 2.63%, 3.03%, 1.76%, 2.79%, 1.96%, and 22.01% false positive rate in lane detection in a daytime driving environment as shown in Table 4, respectively. Although it was noticed that the worn lane markings in clips #1-#5 and #7-#9 are more significant than the other clips in a daytime driving environment, still the lane detection rate in clips #1, #3, #7, #8, and #9 are maintained above 94%. In fact, the worn lane markings found in clips #1-#5 and #7-#9 were only applied on small portion of the printed lane markings on road surface and still visible in a daytime driving environment. Nevertheless, VBLD is still capable to detect the worn lane markings successfully in moderate to heavy traffic flow. It is also observed that the shadow of moving vehicle as shown in Fig. 20d does not

Table 2
Road footage descriptions for lane detection and lane departure detection in a daytime driving environment.

Clip no.	Traffic	Lane marking type	Road surface condition	No. of frame	No. of lane
1 (Em, 2018a)	Moderate	Solid, broken, straight	Occluded lane markings, worn lane markings	1946	7784
2 (Em, 2018b)	Heavy	Solid, broken, straight, curved	Occluded lane markings, other road markings, worn lane markings	3296	13184
3 (Em, 2018c)	Light	Solid, broken, straight, curved	Occluded lane markings, other road markings, wet, worn lane markings, reflections	4496	13488
4 (Em, 2018d)	Moderate	Solid, broken, straight	Occluded lane markings, wet, worn lane markings, reflections	1556	4668
5 (Em, 2019s)	Light	Solid, broken, straight, curved	Occluded lane markings, other road markings, glare, worn lane markings, reflections	7049	22802
6 (Em, 2019t)	Very heavy	Solid, broken, straight, curved	Other road markings, reflections	2400	8021
7 (Em, 2019u)	Moderate	Solid, broken, straight, curved	Other road markings, occluded lane markings, worn lane markings	8400	28098
8 (Em, 2019v)	Moderate	Solid, broken, straight, curved	Other road markings, occluded lane markings, worn lane markings	2550	8827
9 (Em, 2019w)	Heavy	Solid, broken, straight, curved	Other road markings, occluded lane markings, worn lane markings	3750	12335
10 (Em, 2019a)	Moderate	Solid, broken, straight, curved	Other road markings, occluded lane markings	2100	6300
11 (Em, 2019b)	Light	Solid, broken, straight	Other road markings, occluded lane markings	2100	6549
12 (Em, 2019c)	Moderate	Solid, broken, straight, curved	Other road markings, occluded lane markings	2520	9820
13 (Em, 2019d)	Light	Solid, broken, straight	Other road markings, occluded lane markings	539	1617
Total				**42702**	**143493**

Table 3
Road footage descriptions for lane detection and lane departure detection in a night-time driving environment.

Clip no.	Traffic	Lane marking type	Road surface condition	No. of frame	No. of lane
14 (Em, 2019e)	Moderate	Solid, broken, straight, curved	Other road markings, occluded lane markings, night glare, worn lane markings	12719	50876
15 (Em, 2019f)	Light	Solid, broken, straight	Other road markings, occluded lane markings, night glare	510	1530
16 (Em, 2019g)	Moderate	Solid, broken, straight, curved	Other road markings, occluded lane markings, night glare	1829	5487
17 (Em, 2019h)	Light	Solid, broken, straight, curved	Other road markings, occluded lane markings, night glare	1079	3237
18 (Em, 2019i)	Light	Solid, broken, straight, curved	Other road markings, night glare	329	987
19 (Em, 2019j)	Light	Solid, broken, straight, curved	Other road markings, occluded lane markings, night glare, worn lane markings	1739	5217
20 (Em, 2019k)	Light	Solid, broken, straight, curved	Other road markings, occluded lane markings, night glare	239	717
21 (Em, 2019l)	Light	Solid, broken, straight, curved	Other road markings, occluded lane markings, night glare	869	2607
22 (Em, 2019m)	Light	Solid, broken, straight, curved	Other road markings, occluded lane markings, night glare	630	1890
23 Em (2019n)	Light	Solid, broken, straight, curved	Other road markings, occluded lane markings, night glare	2070	6210
24 (Em, 2019o)	Light	Solid, broken, straight, curved	Other road markings, occluded lane markings, night glare	900	2700
25 (Em, 2019p)	Light	Solid, broken, straight, curved	Other road markings, occluded lane markings, night glare, worn lane markings	2550	7650
26 (Em, 2019q)	Light	Solid, broken, straight, curved	Other road markings, occluded lane markings, other road markings, night glare, worn lane markings	720	2160
27 (Em, 2019r)	Moderate	Solid, broken, straight, curved	Other road markings, occluded lane markings, night glare, worn lane markings	1079	3237
Total				**27262**	**94505**

Table 4
Lane detection results for VBLD in a daytime driving environment.

Clip no.	No. of detected lane	No. of correctly detected lane	Lane detection rate, %	No. of false positive lane	False positive rate, %
1	3892	3754	96.45	138	3.55
2	6592	5680	86.17	912	13.83
3	8992	8770	97.53	222	2.47
4	3112	2838	91.20	274	8.80
5	14094	13212	93.74	882	6.26
6	4800	4669	97.27	131	2.73
7	16796	15886	94.57	912	5.43
8	5100	4966	97.37	134	2.63
9	7500	7273	96.97	227	3.03
10	4200	4126	98.24	74	1.76
11	4200	4083	97.21	117	2.79
12	5039	4940	98.04	99	1.96
13	1077	840	77.99	237	22.01
Total	**85394**	**81035**	**94.06**	**4359**	**5.94**

affect the lane detection result of VBLD. Fig. 20d shows correct lane detection, which contained shadow of moving vehicle under daytime and heavy raining driving environment.

Frame images of correct lane detection for lane markings can be seen at frames 1183, 1341, 1356, 1341, 6776, 0564, 7437, 1696, 0110, 0255, 1224, 1397, and 0365 in clips #1-#13, as shown in Figs. 20a-20m, respectively. Whereas, frame images of false positive lane detection, such as a worn lane markings, wet road surface, other road markings like arrow sign painted on the road surface, occluded lane markings, junction box, glare, and reflections shown in Figs. 21a-21m were observed at frames 1511, 0373, 4480, 0231, 2915, 1718, 7298, 1004, 0398, 0378, 1910, 2000, and 0231 in clips #1-#13, respectively.

In clips #14-#27, 97.57%, 96.96%, 97.92%, 98.66%, 98.48%, 89.13%, 95.19%, 99.54%, 96.75%, 97.22%, 98.56%, 88.51%, 90.00%, and 90.59% of 25438, 1020, 3658, 2158, 658, 3478, 478, 1738, 1260, 4140, 1800, 5100, 1440, and 2158 lanes were detected correctly, with 2.43%, 3.04%, 2.13%, 1.34%, 1.52%, 10.87%, 4.81%, 0.46%, 3.25%, 2.78%, 1.44%, 11.49%, 10.00%, and 9.41% false positive rate in lane detection in a night-time driving environment as shown in Table 5, respectively. Although the driving environment in clips #14-#27 were at night-time environment, and clips #1-#13 were at daytime, still the lane detection rates in night-time driving environment are comparable to those of clips in daytime driving environment. Hence, the driving environment isn't an important factor affecting the performance of the lane detection. Instead, sufficient illumination in ROI for revealing the road features like lane markings is an essential factor to be considered in determining the performance of VBLD in a night-time driving environment. Besides, VBLD was also successfully detected the lane markings as shown in Fig. 22c, particularly in total darkness driving environment with only illumination comes from vehicle headlights. Based on observation, majority of frame images in clips #14-#18 and #21-#24 were under sufficient illumination from the road lamps, which resulted above 96% lane detection rate in a night-time driving environment. In addition, the quality of the road surface conditions, such as the clearness of the road features like lane markings and sufficient illumination to reveal the road surface conditions, were fundamentally better on highway compared to urban roads.

Frame images of correct lane detection for lane markings can be seen at frames 04079, 0070, 0144, 0713, 0270, 0758, 0077, 0119,

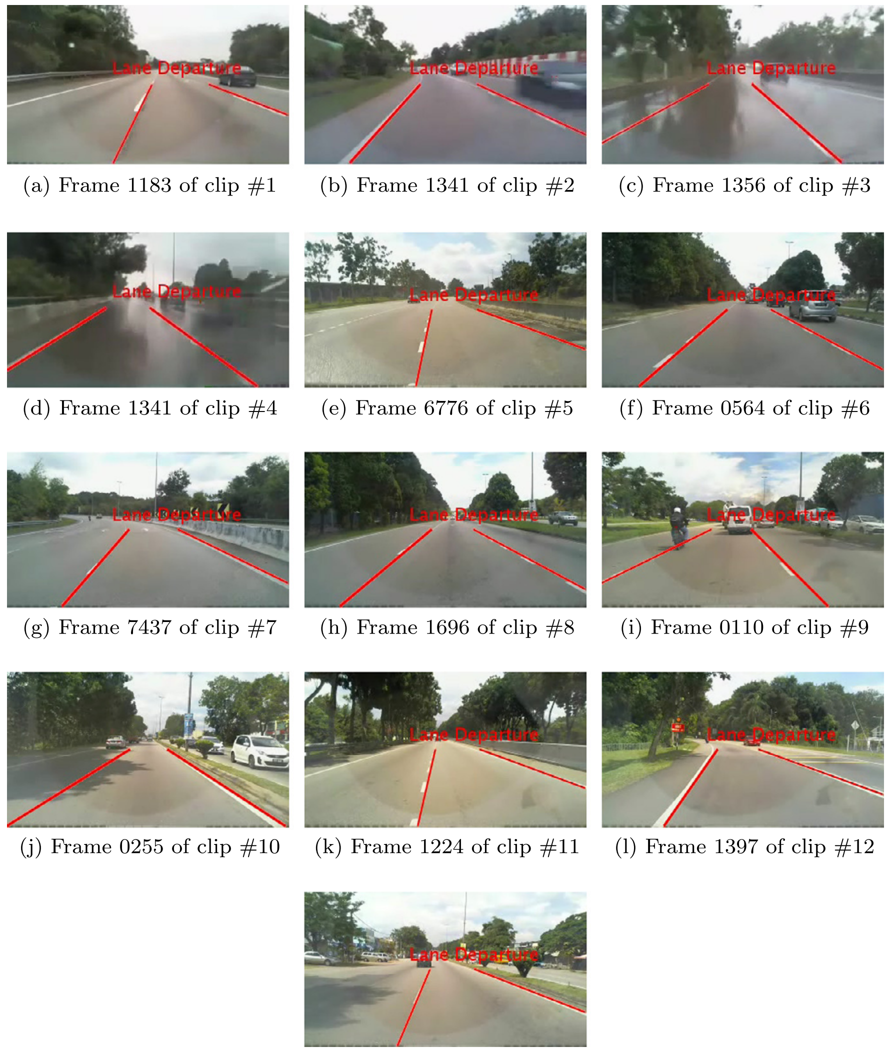

(a) Frame 1183 of clip #1 (b) Frame 1341 of clip #2 (c) Frame 1356 of clip #3

(d) Frame 1341 of clip #4 (e) Frame 6776 of clip #5 (f) Frame 0564 of clip #6

(g) Frame 7437 of clip #7 (h) Frame 1696 of clip #8 (i) Frame 0110 of clip #9

(j) Frame 0255 of clip #10 (k) Frame 1224 of clip #11 (l) Frame 1397 of clip #12

(m) Frame 0365 of clip #13

Fig. 20. Frame images of correct lane detection and lane departure detection in a daytime driving environment using VBLDW.

0066, 1653, 0096, 2497, 0131, and 0125 in clips #14-#27, as shown in Figs. 22a-22n, respectively. Frame images of false positive lane detection, such as the worn lane markings, occluded lane markings, night glare, and other road markings like arrow sign shown in Figs. 23a-23n, were detected at frames 06224, 0184, 1814, 0227, 0293, 0466, 0201, 0025, 0319, 0097, 0887, 1913, 0305, and 0741 in clips #14-#27, respectively. The experiment results show the effectiveness of VBLD in detecting lane markings under challenging driving environments. In average, 94.06% and 95.36% of lane markings were detected correctly in daytime and night-time driving environments, respectively.

The lane departure detection results based on VBLDW in daytime and night-time driving environments are presented in Tables 6, 7, respectively. For the performance evaluation of lane departure detection, the number of lane departure frame, the number of detected lane departure frame, and the number of false positive frame were counted manually on a frame to frame basis. Equations (11), (12), and (13) represent the formulas used for total number of lane departure frame, detection rate, and false positive rate, respectively.

$$N_{TL} = N_{DL} + N_{FL} \tag{11}$$

$$\text{Lane departure detection rate} = \frac{N_{DL}}{N_{TL}} \times 100\% \tag{12}$$

$$\text{False positive rate in lane departure detection} = \frac{N_{FL}}{N_{TL}} \times 100\% \tag{13}$$

Where

N_{TL} - Total number of detected lane departure frame.
N_{DL} - Total number of correctly detected lane departure frame.
N_{FL} - Total number of false positive lane departure frame.

In clips #1-#13, 85.10%, 76.50%, 83.92%, 46.60%, 86.44%, 95.56%, 93.78%, 61.25%, 97.44%, 0.00%, 100.00%, 95.66%, and 100.00% of 302, 783, 566, 221, 2020, 789, 3156, 80, 469, 20, 831, 806,and 359 lane departure frames were detected correctly with 14.90%, 23.50%, 16.08%, 53.40%, 13.56%, 4.44%, 6.22%, 38.75%, 2.56%, 100.00%, 0.00%, 4.34% and 0.00% false positive rate in a daytime driving environment, respectively. Although clip #10 was found to have zero lane departure detection rate, but the number of falsely detected lane departure frames were insignificant (20 frames) to be considered in statistical analysis. Nevertheless, clips #6, #9, #11, #12, and #13 achieved above 95% lane departure detection rate in a daytime driving environment.

Frame images of correct lane departure detection can be seen at frames 1183, 1341, 1356, 1341, 6776, 0564, 7437, 1696, 0110, 0255, 1224, 1397, and 0365 in clips #1-#13, shown in Figs. 20a-20m, respectively. Frame images of false positive lane departure detection can be seen at frames 1511, 0373, 4480, 0231, 2915, 1718, 7298, 1004, 0398, 0378, 1910, 2000, and 0231 in clips #1-#13, shown in Figs. 21a-21m, respectively. The falsely detected arrow sign painted on the road surface, occluded lane markings, and worn lane markings

(a) Frame 1511 of clip #1 (b) Frame 0373 of clip #2 (c) Frame 4480 of clip #3
(d) Frame 0231 of clip #4 (e) Frame 2915 of clip #5 (f) Frame 1718 of clip #6
(g) Frame 7298 of clip #7 (h) Frame 1004 of clip #8 (i) Frame 0398 of clip #9
(j) Frame 0378 of clip #10 (k) Frame 1910 of clip #11 (l) Frame 2000 of clip #12
(m) Frame 0231 of clip #13

Fig. 21. Frame images of false positive lane detection and lane departure detection results in a daytime driving environment using VBLDW.

Table 5
Lane detection results for VBLD in a night-time driving environment.

Clip no.	No. of detected lane	No. of correctly detected lane	Lane detection rate, %	No. of false positive lane	False positive rate, %
14	25438	24821	97.57	617	2.43
15	1020	989	96.96	31	3.04
16	3658	3582	97.92	78	2.13
17	2158	2129	98.66	29	1.34
18	658	648	98.48	10	1.52
19	3478	3100	89.13	378	10.87
20	478	455	95.19	23	4.81
21	1738	1730	99.54	8	0.46
22	1260	1219	96.75	41	3.25
23	4140	4025	97.22	115	2.78
24	1800	1774	98.56	26	1.44
25	5100	4514	88.51	586	11.49
26	1440	1296	90.00	144	10
27	2158	1955	90.59	203	9.41
Total	**54524**	**52237**	**95.36**	**2289**	**4.64**

were the root cause of false positive lane departure detection, which contributed an incorrect LOR computation. Hence, ‘Lane Departure’ text was wrongly displayed in those frame images, in spite of the fact that the vehicle was at the centre of the lane. It was also noticed that the lane departure detection results using VBLD are highly reliant on the lane detection results using the prior VBLD in a daytime driving environment.

In clips #14-#27, 80.44%, 90.65%, 87.95%, 91.89%, 93.46%, 55.64%, 94.21%, 96.28%, 96.04%, 90.59%, 87.65%, 68.29%, 75.09%, and 64.00% of 2295, 107, 498, 148, 153, 692, 121, 188, 328, 818, 170, 905, 273, and 400 lane departure frames were detected correctly, with 19.56%, 9.35%, 12.05%, 8.11%, 6.54%, 44.36%, 5.79%, 3.72%, 3.96%, 9.41%, 12.35%, 31.71%, 24.91%, and 36.00% false positive rate in a night-time driving environment, respectively. It was observed that the

(a) Frame 04079 of clip #14

(b) Frame 0070 of clip #15

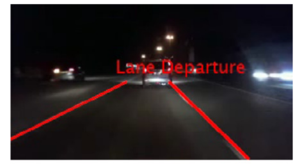

(c) Frame 0144 of clip #16

(d) Frame 0713 of clip #17

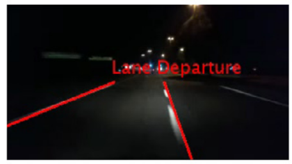

(e) Frame 0270 of clip #18

(f) Frame 0758 of clip #19

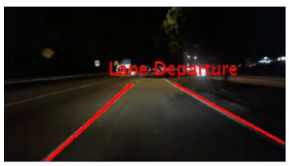

(g) Frame 0077 of clip #20

(h) Frame 0119 of clip #21

(i) Frame 0066 of clip #22

(j) Frame 1653 of clip #23

(k) Frame 0096 of clip #24

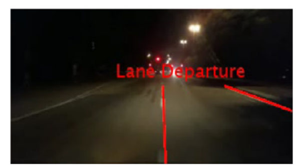

(l) Frame 2497 of clip #25

(m) Frame 0131 of clip #26

(n) Frame 0125 of clip #27

Fig. 22. Frame images of correct lane detection and lane departure detection results in a night-time driving environment using VBLDW.

lane departure detection performance deteriorated under conditions of low illumination, which reflects the independence of VBLDW's lane departure detection results from the prior algorithm. In fact, illumination that is insufficient to reveal the condition of the road features was the essential factor that contributed to the higher false positive rate of lane departure detection in a total darkness driving environment. Thus, this error propagated into the LOR computation, which resulted falsely LDW albeit the driven vehicle was at the centre of the lane.

Frame images of correct lane departure detection can be seen at frames 04079, 0070, 0144, 0713, 0270, 0758, 0077, 0119, 0066, 1653, 0096, 2497, 0131, and 0125 in clips #14-#27, shown in Fig. 22a-22n, respectively. Frame images of false positive lane departure detection can be seen at frames 06224, 0184, 1814, 0227, 0293, 0466, 0201, 0025, 0319, 0097, 0887, 1913, 0305, and 0741 in clips #14-#27, as shown in Fig. 23a-23n, respectively. In spite of the fact that the vehicle was being driven in the centre of the lane, the worn lane markings, falsely detected vehicle from the side, falsely detected arrow sign, and tree shadows found in clips #14-#27 had caused false positive lane departure detection. Thus, 'Lane Departure' text was wrongly displayed in those frame images. The experiment results show the effectiveness of VBLDW in detecting lane departures under challenging driving environments namely daytime and night-time. In average, 78.63% and 83.73% of lane departures were detected correctly in daytime and night-time driving environments, respectively.

4.2. Comparison of lane detection and lane departure detection

FIRSA and benchmark lane marking segmentation methods are implemented and included in Table 8 for comparative performance evaluation using clips #1-#4. The benchmark methods use lane marking segmentation method found on the Canny, Sobel, Prewitt, and Roberts algorithms, followed by Hough transform to detect lane markings. Table 8 shows that the FIRSA lane marking segmentation method performs better than the benchmark lane marking segmentation methods for clips #1 and #3, which represents a common situations in the highway and urban roads, respectively. In spite of highest lane detection rate in clips #1 and #3, FIRSA lane marking segmentation method possesses some instability when it comes to clip #2, which achieving lane detection rate of 86.17% and false positive rate of 13.83%. FIRSA lane marking segmentation method encountered slightly higher false positive rate mainly due to the incorrect lane marking detection, particularly the one on the right lane marking as illustrated in Fig. 21b. Instead of detecting the right lane marking for driving direction, the FIRSA lane marking segmentation method falsely detected the right lane marking for oncoming driving direction. Hence, the false positive detection result. Clip #4 brings a slight advantage in favour of Roberts lane marking segmentation method, while in other two scenarios in clips #1 and #3, the FIRSA lane marking segmentation method seems to have better performance than Roberts method. This situation can be related to the poor illumination during heavy rain weather and unpredictable illumina-

(a) Frame 06224 of clip #14 (b) Frame 0184 of clip #15 (c) Frame 1814 of clip #16
(d) Frame 0227 of clip #17 (e) Frame 0293 of clip #18 (f) Frame 0466 of clip #19
(g) Frame 0201 of clip #20 (h) Frame 0025 of clip #21 (i) Frame 0319 of clip #22
(j) Frame 0097 of clip #23 (k) Frame 0887 of clip #24 (l) Frame 1913 of clip #25
(m) Frame 0305 of clip #26 (n) Frame 0741 of clip #27

Fig. 23. Frame images of false positive lane detection and lane departure detection results in a night-time driving environment using VBLDW.

Table 6
Lane departure detection results for VBLDW in a daytime driving environment.

Clip no.	No. of detected lane departure frame	No. of correctly detected lane departure frame	Lane departure detection rate, %	No. of false positive lane departure frame	False positive rate, %
1	302	257	85.10	45	14.90
2	783	599	76.50	184	23.50
3	566	475	83.92	91	16.08
4	221	103	46.60	118	53.40
5	2020	1746	86.44	274	13.56
6	789	754	95.56	35	4.44
7	3166	2969	93.78	197	6.22
8	80	49	61.25	31	38.75
9	469	457	97.44	12	2.56
10	20	0	0.00	20	100.00
11	831	831	100.00	0	0.00
12	806	771	95.66	35	4.34
13	359	359	100.00	0	0.00
Total	**10412**	**9370**	**78.63**	**1042**	**21.37**

tion interference of vehicles. Hence, FIRSA lane marking segmentation method may perform poorly than it does during sunny weather, which is reflected experimentally in Table 8. It is concluded that, during rainy weather, the successfulness of VBLD using FIRSA lane marking segmentation method mainly depends on clarity of the printed lane markings on road surface and sometimes depend on illumination availability on the road.

In order to verify the validity of VBLD's lane detection results in subsection 4.1, Caltech lanes dataset (Aly, 2008) has been chosen for lane detection methods comparison due to its widely used in lane detection research for comparative studies. The Caltech lanes dataset consists of four clips (cordova1, cordova2, washington1, and washington2) totaling 1225 frames in the size of 640×480, which include many types of complex traffic scenes, namely tree shadows, passing vehicles, and

Table 7
Lane departure detection results for VBLDW in a night-time driving environment.

Clip no.	No. of detected lane departure frame	No. of correctly detected lane departure frame	Lane departure detection rate, %	No. of false positive lane departure frame	False positive rate, %
14	2295	1846	80.44	449	19.56
15	107	97	90.65	10	9.35
16	498	438	87.95	60	12.05
17	148	136	91.89	12	8.11
18	153	143	93.46	10	6.54
19	692	385	55.64	307	44.36
20	121	114	94.21	7	5.79
21	188	181	96.28	7	3.72
22	328	315	96.04	13	3.96
23	818	741	90.59	77	9.41
24	170	149	87.65	21	12.35
25	905	618	68.29	287	31.71
26	273	205	75.09	68	24.91
27	400	256	64.00	144	36.00
Total	**7096**	**5624**	**83.73**	**1472**	**16.27**

Table 8
Comparison of lane marking segmentation methods for clips #1-#4.

Clip	Method	Lane detection rate, %	False positive rate, %
1	**FIRSA**	**96.45**	**3.55**
1	Canny	43.63	56.37
1	Sobel	74.20	25.80
1	Prewitt	72.61	27.39
1	Roberts	76.57	23.43
2	**FIRSA**	**86.17**	**13.83**
2	Canny	64.08	35.92
2	Sobel	90.66	9.34
2	Prewitt	89.96	10.04
2	Roberts	91.66	8.34
3	**FIRSA**	**97.53**	**2.47**
3	Canny	31.94	68.06
3	Sobel	95.86	4.14
3	Prewitt	95.75	4.25
3	Roberts	96.71	3.29
4	**FIRSA**	**91.20**	**8.80**
4	Canny	24.87	75.13
4	Sobel	90.49	9.51
4	Prewitt	89.65	10.35
4	Roberts	92.29	7.71

Table 9
Caltech lanes dataset descriptions.

Clip	Traffic	Lane marking type	Road surface condition	No. of frame	No. of lane
cordova1	Light	Solid, broken, straight, curved	Occluded lane markings, other road markings, worn lane markings	250	919
cordova2	Light	Solid, broken, straight, curved	Occluded lane markings, other road markings, glare, worn lane markings	406	1048
washington1	Moderate	Solid, broken, straight	Occluded lane markings, other road markings, glare	337	1274
washington2	Light	Solid, broken, straight	Occluded lane markings, other road markings	232	931
Total				**1225**	**4172**

Table 10
Lane detection results for VBLD using Caltech lanes dataset.

Clip	No. of detected lane	No. of correctly detected lane	Lane detection rate, %	No. of false positive lane	False positive rate, %
cordova1	500	465	93.00	35	7.00
cordova2	812	690	84.98	122	15.02
washington1	674	607	90.06	67	9.94
washington2	464	437	94.18	27	5.82
Total	**2450**	**2199**	**90.55**	**251**	**9.45**

other road markings. Table 9 tabulates the clips description of Caltech lanes dataset.

For lane detection comparison under Caltech lanes dataset, similar evaluation metrics are used, namely lane detection rate and false positive rate in lane detection in Equations (9)-(10), respectively. The results show the effectiveness of VBLD in detecting lanes on urban streets with varying conditions, which achieved an average of 90.55% lane detection rate and 9.45% false positive rate results under Caltech lanes dataset as shown in Table 10. cordova2 clip obtained lowest lane detection rate and highest false positive rate among the four clips due to false positives were mostly found for right lane of the street with no right lane boundary (Aly, 2008). Hence, VBLD detects the curb as the right lane boundary, which resulted higher false positive rate and lower lane detection rate for cordova2 clip. For washington1 clip, most of the false positives were detected under heavy tree shadows at the beginning frames, which contributed 9.94% false positive rate in lane detection.

(a) Frame f00230 in cordova1 clip (b) Frame f00266 in cordova2 clip (c) Frame f00067 in washington1 clip (d) Frame f00065 in washington2 clip

Fig. 24. Samples of correct lane detection results of VBLD under Caltech lanes dataset.

(a) Frame f00080 in cordova1 clip (b) Frame f00207 in cordova2 (c) Frame f00008 in washington1 clip (d) Frame f00101 in washington2 clip

Fig. 25. Samples of false positive lane detection results of VBLD under Caltech lanes dataset.

Table 11
The performance comparison of different lane detection methods under Caltech lanes dataset (Aly, 2008).

Method	Average lane detection rate, %	Average false positive rate, %	Environment	Runtime, ms
Aly (2008)	96.30	12.08	– (OpenCV + C++)	191
Ye et al. (2018)	98.48	2.43	2 cores @ 3.50 GHz (Matlab)	121
Gupta and Choudhary (2018)	97.28	1.75	2 cores @ 3.00 GHz (OpenCL + C++)	29.7
Hoang et al. (2017)	87.50	12.34	6 cores @ 3.47 GHz (OpenCV + C++)	26.1
Kim et al. (2017)	98.55	–	4 cores @ 3.6 GHz	10-13 min (training time)
Niu et al. (2016)	96.33	2.85	4 cores @ 2.83 GHz (C++)	19.9
Hou et al. (2016)	92.50	5.85	2 cores @ 2.30 GHz (OpenCV + C++)	180
Shin et al. (2015)	92.78	–	4 cores @ 3.30 GHz (OpenCV + C++)	60.7
Guo et al. (2015)	95.75	9.91	2 cores @ 3.0 GHz	40
Liu and Li (2013)	93.15	4.67	2 cores @ 2.53 GHz (Matlab)	400
Ruyi et al. (2011)	95.90	2.40	2 cores @ 2.5 GHz (OpenCV + C)	62
VBLD	**90.55**	**9.45**	**4 cores @ 1.6GHz (Matlab)**	**13**
VBLD with real-life datasets	**94.71**	**5.29**	**4 cores @ 1.6GHz (Matlab)**	**4.9**

For cordova1 and washington2 clips, both achieved higher lane detection rate above 93.00% under clear conditions except cross stop lines and cross walks that contributed into false positives in lane detection. Figs. 24, 25 show samples of correct and false positive lane detection results of VBLD for each clip under Caltech lanes dataset, respectively.

Beside VBLD, other well-known lane detection methods were also compared under Caltech lanes dataset in similar evaluation metrics, namely lane detection rate and false positive rate. Since Caltech lanes dataset consists of four individual clips, the respective clip's lane detection rate and false positive rate were averaged. Table 11 shows the performance comparison of different lane detection methods under Caltech lanes dataset. The comparison was based on two-lane mode. Other than evaluation metrics, environment and runtime were also considered in lane detection methods comparison in Table 11. The runtime represents the average computation time to process one frame.

The comparison was carried out in two-lane mode, which the lane detection only applied to the two boundaries of the host lane on Caltech lanes dataset. VBLD results were compared with the lane detection methods described by Aly (2008); Ye et al. (2018); Gupta and Choudhary (2018); Hoang et al. (2017); Kim et al. (2017); Niu et al. (2016); Hou et al. (2016); Shin et al. (2015); Guo et al. (2015); Liu and Li (2013); Ruyi et al. (2011) under Caltech lanes dataset. The main reason for selecting Aly (2008) works is because Aly generated the public Caltech lanes dataset for evaluation and most of the researchers evaluated performance of their lane detection method using this dataset. As shown in Table 11, the average lane detection rate of VBLD was 8% lower than the state-of-the-art lane detection method in Kim et al. (2017) and most of the lane detection methods in Table 11. It is mostly due to state-of-the-art lane detection methods used sophisticated processing environment such as higher processor clock speed per core count and some methods like Gupta and Choudhary (2018); Hou et al. (2016); Shin et al. (2015); Ruyi et al. (2011) applied tracking stage after detection stage for enhancing lane detection rate. However, VBLD outperforms most of the state-of-the-art lane detection methods in runtime evaluation. The average computation time of VBLD under Caltech lanes dataset is 13 ms in 640×480 image resolution. Some of state-of-the-art lane detection methods used top-view based approach for enhancing lane detection rate, which required intensive computing power for Inverse Perspective Mapping (IPM) and prolonged the runtime per frame. Hence, lane detection method with shorter runtime like VBLD is an ideal for real time implementation for lane detection application. Most of the state-of-the-art lane detection methods were implemented in a highly optimised environment like OpenCV and C++, which resulted better lane detection rates in Table 11. In addition, the field of view (FOV) for real-life datasets is different compared to the FOV of Caltech lanes dataset. For comparison, real-life datasets contained narrow FOV. Whereas, Caltech lanes dataset contained wider FOV. Hence, FOV of the camera does affect the lane detection results of VBLD, preferably the narrower FOV yielded better lane detection than wider FOV. Wider FOV may resulted poorer lane detection results due to outliers.

VBLD not only is used to compare with the state-of-the-art lane detection methods under Caltech lanes dataset, VBLD with real-life datasets is also presented in Table 11 for verifying the validity of lane detection results generated in subsection 4.1. Table 11 shows that VBLD achieved comparable results in average lane detection rate at above 90% and less than 10% of average false positive rate for both datasets. It is noted that real-life datasets contained smaller resolution frame images at 320×180 and resulted shorter average runtime per frame at

Table 12
Overall lane departure detection results for VBLDW under real-life datasets.

Method	Average lane departure detection rate, %		Average false positive rate in lane departure detection, %		Environment	Runtime, ms
	Daytime	Night-time	Daytime	Night-time		
VBLDW	78.63	83.73	21.37	16.27	4 cores @ 1.6GHz (Matlab)	5.1

4.9 ms. The main purpose for performance comparison of different lane detection methods in Table 11 isn't completing with the state-of-the-art lane detection methods in evaluation metrics but to provide a mean for identifying the reference points of VBLD in term of evaluation metrics, environment, and runtime compared to the state-of-the-art lane detection methods under similar dataset.

As for lane departure detection comparison, non of public or well-known datasets were identified for providing fair comparison with VBLDW. Hence, VBLDW's lane departure detection results generated in subsection 4.1 were presented here under real-life datasets. Real-life datasets consist of 69964 frames of road footage for lane departure detection analysis for clips #1-#27. Since real-life datasets consists of 27 individual clips, the respective clip's lane departure detection rate and false positive rate in lane departure rate were averaged. Out of the total road footage frames, 17508 frames were belong to lane departure warning frames in VBLDW.

Table 12 presents the overall lane departure detection results for VBLDW. It can be seen that daytime and night-time driving environments were considered in VBLDW in terms of the lane departure detection rate and false positive rate in lane departure detection analysis. In a daytime driving environment, VBLDW achieved an average of 78.63% lane departure detection rate and 21.37% false positive rate in lane departure detection under real-life datasets. However, in a night-time driving environment, VBLDW contributed an average of 83.73 % lane departure detection rate and 16.27% false positive rate in lane departure detection. Although the results show the consistency of VBLDW in lane departure detection under variation of driving environments, however, the false positive rate in lane departure detection using VBLDW is still consider higher at above 16% due to limitation of vision system in overcoming the disturbances such as worn lane markings, low illumination, other road markings like arrow sign, occluded lane markings, and tree shadows.

5. Conclusion

In this paper, a vision-based lane departure warning (VBLDW) framework has been presented, composed of a vision-based lane detection (VBLD) framework followed by a computation of the lateral offset ratio. VBLDW has two stages: pre-processing and detection. In the pre-processing stage, a colour space conversion, an extraction of the region of interest, and a finite impulse response saturation autothreshold lane marking segmentation method are implemented, in that order. In the detection stage, the Hough transformation and peak detection, reverse Hough transformation, and the drawing of the detected lines in the original image are implemented. Lastly, the lateral offset ratio is computed for determining whether to issue a lane departure warning. This computation is based on the detected X-coordinates of the bottom end-points of each lane boundary in the image plane. Road footage from urban roads and a highway in the city of Malacca were collected for evaluating the performance in lane detection and lane departure detection. The lane detection rate and the false positive rate were studied. An average of lane detection rates of 94.06% and 95.36% were achieved in daytime and night-time driving environments, respectively. The corresponding false positive detection rates were 5.94% and 4.64%, respectively. The experimental results show the effectiveness of the VBLD in detecting lanes under challenging driving conditions, namely daytime and night-time. It has been seen from the evaluation of the performance of this method for lane detection that neither the driving environment nor the traffic flow are the essential factors affecting the performance of the proposed VBLD. Instead, road surface conditions, particularly worn lane markings, were found to be the main contributor to the false positive rate. Benchmark lane marking segmentation methods were also implemented and compared with FIRSA lane marking segmentation method in clips #1-#4. Overall, FIRSA lane marking segmentation method achieved higher lane detection rate and lower false positive rate than benchmark lane marking segmentation methods. Besides real-life datasets, a well-known Caltech lanes dataset was used for lane detection comparison with state-of-the-art lane detection methods. In average, VBLD achieved 90.55% lane detection rate and 9.45% false positive rate under Caltech lanes dataset. In the evaluation of the lane departure detection, detection rates of 78.63% and 83.73% were obtained in daytime and night-time driving environments, respectively. The corresponding false positive rates were 21.37%, and 16.27%, respectively. The experimental results show the effectiveness of the proposed VBLDW in detecting lane departures in daytime and night-time driving environments. Although the lane departure detection performs better in a night-time driving environment, low illumination under night-time driving conditions resulted in a lower lane departure detection rate, as observed in clips #14 and #25. In a night-time driving environment, the false positive rate was intensified when there were worn lane markings. Nevertheless, based on the experimental results, the proposed system performed effectively under daytime driving environment except clip #4 under heavy rain weather. However, in real-world situations, low illumination and road surface interference are often encountered in our daily driving. Thus, a vision-based system, especially the lane detection system proposed in this paper as well as the proposed VBLDW system, fall short in terms of their reliability under complex driving environments and road surface conditions. The examples of complex driving environments and road surface conditions encountered in the experiments were low illumination at night, worn lane markings, arrow signs, and occluded lane markings. Future research should include mainly the coverage of all-weather test environments. As a part of an intelligent transportation system, lane detection performance can be further enhanced with inclusion of tracking elements for smoother lane detection results. Also, the vehicle's dynamical state can be retrieved to enhance the lane departure detection rate in various road conditions.

Declarations

Author contribution statement

Em Poh Ping: Conceived and designed the experiments; Performed the experiments; Analysed and interpreted the data; Contributed reagents, materials, analysis tools or data; Wrote the paper.

J. Hossen: Conceived and designed the experiments.

Fitrian Imaduddin: Conceived and designed the experiments.

Wong Eng Kiong: Conceived and designed the experiments.

Funding statement

The research described in this paper was supported by Multimedia University (MMU) Mini Fund (Grant No. MMUI/180170) and the Malaysian Ministry of Higher Education (MOHE) for Fundamental Research Grant Scheme (FRGS/1/2018/TK03/MMU/02/1).

Competing interest statement

The authors declare no conflict of interest.

Additional information

Supplementary content related to this article has been published online at:

Clip #1. URL: https://data.mendeley.com/datasets/rkyfwv9hw8/1, https://doi.org/10.17632/RKYFWV9HW8.1.

Clip #2. URL: https://data.mendeley.com/datasets/ynmympptmy/1, https://doi.org/10.17632/YNMYMPPTMY.1.

Clip #3. URL: https://data.mendeley.com/datasets/m88955h7vb/1, https://doi.org/10.17632/M88955H7VB.1.

Clip #4. URL: https://data.mendeley.com/datasets/vry8n5nkrf/1, https://doi.org/10.17632/VRY8N5NKRF.1.

Clip #5. URL: https://data.mendeley.com/datasets/f24x2p6b5h/1, https://doi.org/10.17632/F24X2P6B5H.1.

Clip #6. URL: https://data.mendeley.com/datasets/xskxs82mz6/1, https://doi.org/10.17632/XSKXS82MZ6.1.

Clip #7. URL: https://data.mendeley.com/datasets/dppstzh8n6/2, https://doi.org/10.17632/DPPSTZH8N6.2.

Clip #8. URL: https://data.mendeley.com/datasets/hgt5whhj6n/1, https://doi.org/10.17632/HGT5WHHJ6N.1.

Clip #9. URL: https://data.mendeley.com/datasets/bvbykc4hxf/2, https://doi.org/10.17632/BVBYKC4HXF.2.

Clip #10. URL: https://data.mendeley.com/datasets/g98zzcn6nr/1, https://doi.org/10.17632/G98ZZCN6NR.1.

Clip #11. URL: https://data.mendeley.com/datasets/z3yjbd4567/1, https://doi.org/10.17632/Z3YJBD4567.1.

Clip #12. URL: https://data.mendeley.com/datasets/ytn823rw8j/1, https://doi.org/10.17632/YTN823RW8J.1.

Clip #13. URL: https://data.mendeley.com/datasets/946jzttn7/1, https://doi.org/10.17632/946JZTTN7N.1.

Clip #14. URL: https://data.mendeley.com/datasets/cww75348bj/1, https://doi.org/10.17632/CWW75348BJ.1.

Clip #15. URL: https://data.mendeley.com/datasets/k74tdgbhjm/1, https://doi.org/10.17632/K74TDGBHJM.1.

Clip #16. URL: https://data.mendeley.com/datasets/hps9jsjwxp/2, https://doi.org/10.17632/HPS9JSJWXP.2.

Clip #17. URL: https://data.mendeley.com/datasets/bxmmttx535/1, https://doi.org/10.17632/BXMMTTX535.1.

Clip #18. URL: https://data.mendeley.com/datasets/smx7tbx29p/1, https://doi.org/10.17632/SMX7TBX29P.1.

Clip #19. URL: https://data.mendeley.com/datasets/kcxpm835gw/1, https://doi.org/10.17632/KCXPM835GW.1.

Clip #20. URL: https://data.mendeley.com/datasets/m25z57438h/1, https://doi.org/10.17632/M25Z57438H.1.

Clip #21. URL: https://data.mendeley.com/datasets/cjptbmddpk/2, https://doi.org/10.17632/CJPTBMDDPK.2.

Clip #22. URL: https://data.mendeley.com/datasets/yhd2j7ddxc/1, https://doi.org/10.17632/YHD2J7DDXC.1.

Clip #23. URL: https://data.mendeley.com/datasets/5zjf62drv7/1, https://doi.org/10.17632/5ZJF62DRV7.1.

Clip #24. URL: https://data.mendeley.com/datasets/r8vm7nbgvm/1, https://doi.org/10.17632/R8VM7NBGVM.1.

Clip #25. URL: https://data.mendeley.com/datasets/642n3xx8s6/1, https://doi.org/10.17632/642N3XX8S6.1.

Clip #26. URL: https://data.mendeley.com/datasets/wmymrk79tg/1, https://doi.org/10.17632/WMYMRK79TG.1.

Clip #27. URL: https://data.mendeley.com/datasets/wb4hgnr6k3/1, https://doi.org/10.17632/WB4HGNR6K3.1.

References

Al-Madani, H.M., 2018. Global road fatality trends' estimations based on country-wise micro level data. Accid. Anal. Prev. 111, 297–310.

Aly, M., 2008. Real time detection of lane markers in urban streets. In: IEEE Intelligent Vehicles Symposium, Proceedings, pp. 7–12. arXiv:1411.7113v1.

Chandrasekar, P., Ryu, J.Y., 2016. Design of programmable digital FIR/IIR filter with excellent noise cancellation. Int. J. Appl. Eng. Res. 11, 8467–8470.

Cualain, D.O., Glavin, M., Jones, E., 2012. Multiple-camera lane departure warning system for the automotive environment. IET Intell. Transp. Syst. 6, 223.

Duda, R.O., Hart, P.E., 1972. Use of the hough transformation to detect lines and curves in pictures. Commun. ACM 15, 11–15.

Em, P.P., 2018a. Clip #1. https://data.mendeley.com/datasets/rkyfwv9hw8/1.

Em, P.P., 2018b. Clip #2. https://data.mendeley.com/datasets/ynmympptmy/1.

Em, P.P., 2018c. Clip #3. https://data.mendeley.com/datasets/m88955h7vb/1.

Em, P.P., 2018d. Clip #4. https://data.mendeley.com/datasets/vry8n5nkrf/1.

Em, P.P., 2019a. Clip #10. https://data.mendeley.com/datasets/g98zzcn6nr/1.

Em, P.P., 2019b. Clip #11. https://data.mendeley.com/datasets/z3yjbd4567/1.

Em, P.P., 2019c. Clip #12. https://data.mendeley.com/datasets/ytn823rw8j/1.

Em, P.P., 2019d. Clip #13. https://data.mendeley.com/datasets/946jzttn7n/1.

Em, P.P., 2019e. Clip #14. https://data.mendeley.com/datasets/cww75348bj/1.

Em, P.P., 2019f. Clip #15. https://data.mendeley.com/datasets/k74tdgbhjm/1.

Em, P.P., 2019g. Clip #16. https://data.mendeley.com/datasets/hps9jsjwxp/2.

Em, P.P., 2019h. Clip #17. https://data.mendeley.com/datasets/bxmmttx535/1.

Em, P.P., 2019i. Clip #18. https://data.mendeley.com/datasets/smx7tbx29p/1.

Em, P.P., 2019j. Clip #19. https://data.mendeley.com/datasets/kcxpm835gw/1.

Em, P.P., 2019k. Clip #20. https://data.mendeley.com/datasets/m25z57438h/1.

Em, P.P., 2019l. Clip #21. https://data.mendeley.com/datasets/cjptbmddpk/2.

Em, P.P., 2019m. Clip #22. https://data.mendeley.com/datasets/yhd2j7ddxc/1.

Em, P.P., 2019n. Clip #23. https://data.mendeley.com/datasets/5zjf62drv7/1.

Em, P.P., 2019o. Clip #24. https://data.mendeley.com/datasets/r8vm7nbgvm/1.

Em, P.P., 2019p. Clip #25. https://data.mendeley.com/datasets/642n3xx8s6/1.

Em, P.P., 2019q. Clip #26. https://data.mendeley.com/datasets/wmymrk79tg/1.

Em, P.P., 2019r. Clip #27. https://data.mendeley.com/datasets/wb4hgnr6k3/1.

Em, P.P., 2019s. Clip #5. https://data.mendeley.com/datasets/f24x2p6b5h/1.

Em, P.P., 2019t. Clip #6. https://data.mendeley.com/datasets/xskxs82mz6/1.

Em, P.P., 2019u. Clip #7. https://data.mendeley.com/datasets/dppstzh8n6/2.

Em, P.P., 2019v. Clip #8. https://data.mendeley.com/datasets/hgt5whhj6n/1.

Em, P.P., 2019w. Clip #9. https://data.mendeley.com/datasets/bvbykc4hxf/2.

Guo, J., Wei, Z., Miao, D., 2015. Lane detection method based on improved RANSAC algorithm. In: Proceedings - 2015 IEEE 12th International Symposium on Autonomous Decentralized Systems. ISADS 2015, pp. 285–288.

Gupta, A., Choudhary, A., 2018. Real-time lane detection using spatio-temporal incremental clustering. In: IEEE Conference on Intelligent Transportation Systems, Proceedings. ITSC, pp. 1–6.

Haloi, M., Jayagopi, D.B., 2015. A robust lane detection and departure warning system. In: IEEE Intelligent Vehicles Symposium, Proceedings 2015-Augus, pp. 126–131.

Hoang, T.M., Baek, N.R., Cho, S.W., Kim, K.W., Park, K.R., 2017. Road lane detection robust to shadows based on a fuzzy system using a visible light camera sensor. Sensors 17.

Hou, C., Hou, J., Yu, C., 2016. An efficient lane markings detection and tracking method based on vanishing point constraints. In: Chinese Control Conference. CCC, pp. 6999–7004.

International Organization for Standardization [ISO], 2007. Intelligent transport systems–lane departure warning systems–performance requirements and test procedures. https://www.iso.org/standard/41105.html.

Jacobs, G., Aeron-Thomas, A., 1999. A review of global road accident fatalities. In: RoSPA Road Safety Congress, pp. 1–15.

Jacobs, G., Thomas, A.A., Astrop, A., 2000. Estimating Global Road Fatalities. Technical Report. Department for International Development, London.

Jung, C.R., Kelber, C.R., 2004. A robust linear-parabolic model for lane following. In: Computer Graphics and Image Processing, 2004. Proceedings. 17th Brazilian Symposium on, pp. 72–79.

Jung, C.R., Kelber, C.R., 2005a. A lane departure warning system using lateral offset with uncalibrated camera. In: Intelligent Transportation Systems, Proceedings. IEEE, pp. 102–107.

Jung, C.R., Kelber, C.R., 2005b. An improved linear-parabolic model for lane following and curve detection. In: Computer Graphics and Image Processing, 2005. SIBGRAPI 2005. 18th Brazilian Symposium on, pp. 131–138.

Kim, J.J., Kim, J.J., Jang, G.J.J., Lee, M., 2017. Fast learning method for convolutional neural networks using extreme learning machine and its application to lane detection. Neural Netw. 87, 109–121. http://linkinghub.elsevier.com/retrieve/pii/S0893608016301885.

Kopits, E., Cropper, M., 2005. Traffic fatalities and economic growth. Accid. Anal. Prev. 37, 169–178.

Liu, W., Li, S., 2013. An effective lane detection algorithm for structured road in urban. In: Intelligent Science and Intelligent Data Engineering. IScIDE 2012. In: Lecture Notes in Computer Science. Springer, Heidelberg, pp. 759–767.

Logitech, 2018. Logitech C525 HD Webcam. https://www.logitech.com/en-us/product/hd-webcam-c525.

Lu, G., 2015. A Lane Detection, Tracking and Recognition System for Smart Vehicles. Ph.D. thesis. University of Ottawa.

Marino, R., Scalzi, S., Orlando, G., Netto, M., 2009. A nested PID steering control for lane keeping in vision based autonomous vehicles. In: American Control Conference, pp. 2885–2890.

Meng, F., Spence, C., 2015. Tactile warning signals for in-vehicle systems. Accid. Anal. Prev. 75, 333–346.

Narote, S.P., Bhujbal, P.N., Narote, A.S., Dhane, D.M., 2018. A review of recent advances in lane detection and departure warning system. Pattern Recognit. 73, 216–234.

Niu, J., Lu, J., Xu, M., Lv, P., Zhao, X., 2016. Robust lane detection using two-stage feature extraction with curve fitting. Pattern Recognit. 59, 225–233.
Otsu, N., 1979. A threshold selection method from gray-level histograms. IEEE Trans. Syst. Man Cybern. 9, 62–66.
Risack, R., Mohler, N., Enkelmann, W., 2000. A video-based lane keeping assistant. In: Proceedings of the IEEE Intelligent Vehicles Symposium. Dearborn, MI, pp. 356–361.
Ruyi, J., Reinhard, K., Tobi, V., Shigang, W., 2011. Lane detection and tracking using a new lane model and distance transform. Mach. Vis. Appl. 22, 721–737.
Shah, M., 1997. Fundamental of Computer Vision. Orlando, FL.
Shin, B.S., Tao, J., Klette, R., 2015. A superparticle filter for lane detection. Pattern Recognit. 48, 3333–3345.
Sternlund, S., Strandroth, J., Rizzi, M., Lie, A., Tingvall, C., 2017. The effectiveness of lane departure warning systems—a reduction in real-world passenger car injury crashes. Traffic Injury Prev. 18, 225–229.
Sudhakaran, A., 2017. Lateral Control Using a MobilEye Camera for Lane Keeping Assist. Ph.D. thesis. Eindhoven University of Technology.
Terrell, T., Simpson, R., 1986. Two-dimensional FIR filter for digital image processing. J. Inst. Electr. Radio Eng. 56, 103–106. http://ieeexplore.ieee.org/document/5261456/.
Vacek, S., Schimmel, C., Dillmann, R., 2007. Road-marking analysis for autonomous vehicle guidance. In: EMCR, pp. 1–6.
Viswanath, P., Chitnis, K., Swami, P., Mody, M., Shivalingappa, S., Nagori, S., Mathew, M., Desappan, K., Jagannathan, S., Poddar, D., Jain, A., Garud, H., Appia, V., Mangla, M., Dabral, S., 2016. A diverse low cost high performance platform for advanced driver assistance system (ADAS) applications. In: IEEE Computer Society Conference on Computer Vision and Pattern Recognition Workshops, pp. 819–827.
Wegman, F., 2017. The future of road safety: a worldwide perspective. IATSS Res. 40, 66–71.
Ye, Y.Y., Hao, X.L., Chen, H.J., 2018. Lane detection method based on lane structural analysis and CNNs. IET Intell. Transp. Syst. 12, 513–520. http://digital-library.theiet.org/content/journals/10.1049/iet-its.2017.0143.
Yoshida, H., Omae, M., Wada, T., 2015. Toward next active safety technology of intelligent vehicle. J. Robot. Mechatron. 27, 610–616.